Visualizing alpha-synuclein and iron deposition in M83 mouse model of Parkinson's disease in vivo

Straumann, Nadja ; Combes, Benjamin Francois ; Dean Ben, Xose Luis ; Sternke-Hoffmann, Rebecca ; Gerez, Juan A ; Dias, Ines ; Chen, Zhenyue ; Watts, Benjamin ; Rostami, Iman ; Shi, Kuangyu ; Rominger, Axel ; Baumann, Christian R ; Luo, Jinghui ; Noain, Daniela ; Nitsch, Roger M ; Okamura, Nobuyuki ; Razansky, Daniel ; Ni, Ruiqing

DOI: https://doi.org/10.1111/bpa.13288

Received: 23 December 2023 | Accepted: 26 June 2024

DOI: 10.1111/bpa.13288

RESEARCH ARTICLE

Brain Pathology

Visualizing alpha-synuclein and iron deposition in M83 mouse model of Parkinson's disease in vivo

Nadja Straumann[1] | **Benjamin F. Combes**[1] | **Xose Luis Dean Ben**[2] | **Rebecca Sternke-Hoffmann**[3] | **Juan A. Gerez**[4] | **Ines Dias**[5] | **Zhenyue Chen**[2] | **Benjamin Watts**[6] | **Iman Rostami**[7] | **Kuangyu Shi**[8] | **Axel Rominger**[8] | **Christian R. Baumann**[5] | **Jinghui Luo**[3] | **Daniela Noain**[5] | **Roger M. Nitsch**[1] | **Nobuyuki Okamura**[9] | **Daniel Razansky**[2] | **Ruiqing Ni**[1,2,8]

[1]Institute for Regenerative Medicine, University of Zurich, Zurich, Switzerland

[2]Institute for Biomedical Engineering, University of Zurich & ETH Zurich, Zurich, Switzerland

[3]Department of Biology and Chemistry, Paul Scherrer Institute, Villigen, Switzerland

[4]Laboratory of Physical Chemistry, Department of Chemistry and Applied Biosciences, ETH Zurich, Zurich, Switzerland

[5]Neurology Department, University Hospital Zurich, Zurich, Switzerland

[6]Photon Science Division, Paul Scherrer Institute, Villigen, Switzerland

[7]Microscopic Anatomy and Structural Biology, University of Bern, Bern, Switzerland

[8]Department of Nuclear Medicine, Inselspital, Bern University Hospital, University of Bern, Bern, Switzerland

[9]Division of Pharmacology, Faculty of Medicine, Tohoku Medical and Pharmaceutical University, Sendai, Japan

Correspondence
Ruiqing Ni, Institute for Regenerative Medicine, University of Zurich, Wagistrasse 12, 9th Floor, 8952 Zurich, Switzerland.
Email: ruiqing.ni@uzh.ch

Funding information
National Institutes of Health, Grant/Award Number: R01-NS126102-01; Innosuisse - Schweizerische Agentur für Innovationsförderung, Grant/Award Number: 51767.1 IP-LS; Swiss Center for Applied Human Toxicology, Grant/Award Number: AP22-02; Novartis Stiftung für Medizinisch-Biologische Forschung; Schweizerischer Nationalfonds zur Förderung der Wissenschaftlichen Forschung, Grant/Award Numbers: 310030_192757, 31ND30_213444; Olga Mayenfisch Stiftung; Parkinson Schweiz; Dementia Research Switzerland-Foundation Synapsis, Grant/Award Number: 2018PI-03; Fondation Gustave et Simone Prévot

Abstract

Abnormal alpha-synuclein (αSyn) and iron accumulation in the brain play an important role in Parkinson's disease (PD). Herein, we aim to visualize αSyn inclusions and iron deposition in the brains of M83 (A53T) mouse models of PD in vivo. The fluorescent pyrimidoindole derivative THK-565 probe was characterized by means of recombinant fibrils and brains from 10- to 11-month-old M83 mice. Concurrent wide-field fluorescence and volumetric multispectral optoacoustic tomography (vMSOT) imaging were subsequently performed in vivo. Structural and susceptibility weighted imaging (SWI) magnetic resonance imaging (MRI) at 9.4 T as well as scanning transmission x-ray microscopy (STXM) were performed to characterize the iron deposits in the perfused brains. Immunofluorescence and Prussian blue staining were further performed on brain slices to validate the detection of αSyn inclusions and iron deposition. THK-565 showed increased fluorescence upon binding to recombinant αSyn fibrils and αSyn inclusions in post-mortem brain slices from patients with PD and M83 mice. Administration of THK-565 in M83 mice showed higher cerebral retention at 20 and 40 min post-intravenous injection by wide-field fluorescence compared to nontransgenic littermate mice, in congruence with the vMSOT findings. SWI/phase images and Prussian blue indicated the accumulation of iron deposits in the brains of M83 mice, presumably in the Fe^{3+} form, as evinced by the STXM results. In conclusion, we demonstrated in vivo mapping of αSyn by means of noninvasive epifluorescence and vMSOT

imaging and validated the results by targeting the THK-565 label and SWI/STXM identification of iron deposits in M83 mouse brains ex vivo.

KEYWORDS
alpha-synuclein, fluorescence imaging, iron, magnetic resonance imaging, optoacoustic imaging, Parkinson's disease, susceptibility weighted imaging

1 | INTRODUCTION

Alpha-synucleinopathies such as Parkinson's disease (PD), dementia with Lewy bodies, and multiple system atrophy are some of the most common neurodegenerative diseases [1]. Neuronal inclusions formed by β-sheet-rich fibrillar alpha-synuclein (αSyn), termed Lewy bodies, pale bodies, and Lewy neurites, are pathological hallmarks of PD. The accumulation of misfolded αSyn inclusions precedes the loss of dopaminergic neurons in the substantia nigra and is an important target for early diagnosis [2, 3]. Iron is linked to important biological processes in the brain, such as oxygen transportation and neurotransmitter synthesis [4]. Magnetic resonance imaging (MRI), for example, using T_2* [5, 6], susceptibility weighted imaging (SWI), and quantitative susceptibility mapping (QSM) [7, 8], has demonstrated brain iron accumulation in patients with atypical PD syndromes [9] and PD [10], as well as in animal models of PD imaged in vivo [6]. Abnormal accumulation of iron has been shown to confer neurotoxicity to nigral neurons [11], induce dopaminergic damage [12], and promote αSyn aggregation. In turn, αSyn aggregation disrupts iron metabolism, leading to elevated iron accumulation and redistribution within neurons and promoting ferroptosis in animal models [13, 14].

A few chemical structures and positron emission tomography imaging ligands targeting αSyn have been identified and evaluated in vitro or in animal models (rodents, minipigs, and nonhuman primates) [15]. These include [^{18}F]C05-05, [^{11}C]MODAG-001, [^{11}C]MK-7337, [^{18}F]4FBox, [^{18}F]-F0502B, [^{18}F]AS69 affibody, and antibody-based [^{124}I]RmAbSynO2-scFv8D3 [16–22]. In addition, fluorescence-emitting imaging probes have been developed and evaluated in *post-mortem* human brain tissue with αSyn inclusions [23, 24]. In vivo epifluorescence (epiFL) imaging of αSyn inclusions in animal models has been reported only using rats injected with labeled fluorescent atto-647 αSyn fibrils [25] or in the retinas of mice overexpressing αSyn fused to green fluorescent protein [26]. On the other hand, fluorescence imaging approaches such as 2-photon microscopy and diffuse optical imaging have a limited penetration depth. MRI using ScFv-conjugated superparamagnetic iron oxide nanoparticles W20-SPIONs in A53T mice [27] provided whole-brain coverage despite relatively low sensitivity. Volumetric multispectral optoacoustic tomography (vMSOT) has the unique features of high sensitivity of optical contrast and high spatial resolution (~120 μm) of ultrasound [28–31]. Additionally, it can achieve a penetration depth sufficient to cover the entire mouse brain. This approach provides spectral sensitivity to detect cerebral oxygenation based on intrinsic oxy-/deoxyhemoglobin (HbO_2/Hb) contrast, as well as extrinsically administered molecular agents targeting neuroinflammation, Aβ, and tau deposits in the brain of animal models of neurodegenerative diseases [32, 33].

In this study, we aimed to visualize αSyn and iron deposits in the brains of a transgenic mouse model of PD, the M83 (A53T) line, using concurrent epiFL-vMSOT, high-field MRI, and scanning transmission x-ray microscopy. We utilized the novel pyrimidoindole derivative THK-565 [34] for in vivo imaging of αSyn inclusions. THK-565 is a novel near-infrared fluorescence imaging probe targeting the beta-sheet structure of amyloids [34]. The earlier study has shown its blood–brain barrier (BBB) permeability, and suitable Log*p* value for in vivo imaging in the mouse brain [34]. It has been previously shown in the early study to bind with Aβ deposition in the brain of amyloid precursor protein (APP)-(knock-in) KI mice [34]. Here, we assessed its ability to detect αSyn aggregates in vitro, in vivo in an animal model with cerebral αSyn deposits as well as in post-mortem brain tissue slices from patients with PD.

2 | METHODS

2.1 | Post-mortem human brain tissue

Post-mortem tissue from one non-demented control, one PD patient with a clinical diagnosis confirmed by pathological examination of Lewy bodies (Braak LB 5, without tau and Aβ), as well as one progressive supranuclear palsy (PSP) case and one corticobasal degeneration (CBD) case with 4R-tau inclusions, were included in this study (Table 1). Paraffin-embedded autopsy brain tissues from the medulla oblongata with high αSyn inclusion accumulation were included. All materials had been collected from donors or from whom written informed consent for a brain autopsy had been obtained and the use of the materials and clinical information for research purposes had been obtained by the Netherlands Brain Bank (NBB), Netherlands. The study was conducted according to the principles of the Declaration of Helsinki and subsequent revisions. All experiments on autopsied human

TABLE 1 Information on brain tissue samples from patients with Parkinson's disease and animal models.

Post-mortem human brain sample								
No	**Sex**	**Age (years)**	**PMD (h)**	**Braak tau**	**Amyloid-β**	**Braak LB**	**Diagnosis**	**Region**
1	F	77	2.7	2	O	0	NC	MO
2	M	61	7.5	1	O	6	PD	MO
3	F	83	5.3	3	O	1	PSP	PPI
4	M	69	8.3	2		0	CBD	CP

Mouse brain sample			
Model	**Number of mice**	**Sex**	**Age (m)**
M83 mice	10	M/F	10–11
arcAβ mice	2	M/F	18
pR5 mice	2	M/F	18
Nontransgenic littermate mice[a]	10	M/F	10–11

Abbreviations: CBD, corticobasal degeneration; CP, caudate with putamen; F, female; LB, Lewy body; M, male; MO, medulla oblongata; NC, non-demented control; PD, Parkinson's disease; PMD, post-mortem delay; PPI, putamen with pallidum (insula); PSP, progressive supranuclear palsy.
[a]Nontransgenic littermate mice for M83 mice.

brain tissue were carried out in accordance with ethical permission obtained from the regional human ethics committee in Canton Zurich and the medical ethics committee of the VU Medical Center for the NBB tissue.

2.2 | Animal models

Transgenic mice carrying the A53T-mutated human αSyn gene [35] (M83, both sexes, 10–11 months old, $n = 15$) and nontransgenic littermates (NTLs, both sexes, $n = 9$) were used [35, 36]. Animals were housed in individually ventilated cages inside a temperature-controlled room under a noninverted 12-h dark/light cycle. Two arcAβ transgenic mice [32, 37] overexpressing the human APP695 transgene containing the Swedish (*K670N/M671L*) and Arctic (*E693G*) mutations under the control of the prion protein promoter and two age-matched NTLs of both sexes (18 months of age) were used. Two *MAPT* P301L transgenic mice overexpressing human 2N/4R tau under the neuron-specific Thy1.2 promoter (pR5 line, C57B6. Dg background, 10.5–11 months old) [38–40], and two respective NTL mice were used. Pelleted food (3437PXL15 and CARGILL) and water were provided ad libitum. ARRRIVAL 2.0 was followed for the design of experiments. All experiments were performed in accordance with the Swiss Federal Act on Animal Protection and were approved by the Cantonal Veterinary Office Zurich (license numbers: ZH024/21, ZH162/20).

2.3 | Materials

8-Methyl-10,10-dimethyl-10a-[4-[4-(dimethylamino)phenyl]-1,3,butadienyl]-3,4,10,10-atetrahyro-pyrimido[1,2,a] indol-2(1H)-one (THK-565) was synthesized and kindly provided by Prof. Nobuyuki Okamura (Tohoku University, Japan) (molecular weight 401.56, chemical structure shown in Figure 1A) [34]. Other chemicals and reagents were commercially purchased (details in Table S1).

2.4 | In vitro fluorescence assay for the binding of ligands to recombinant $A\beta_{42}$, K18 tau, and αSyn fibrils

Recombinant $A\beta_{42}$, K18 tau, and αSyn were expressed and produced by *Escherichia coli* as described previously [41–43]. The fluorescent dyes were dissolved in Milli-Q H_2O or dimethyl sulfoxide (DMSO) and further diluted in 1× phosphate buffered saline (PBS), pH 7.4. The absorbance of the compounds was measured. Thioflavin T assays against $A\beta_{42}$ and K18 tau and αSyn fibrils were performed as described previously [41, 43, 44], with two independent experiments and three technical replicates (Fluoromax 4, Horiba Scientific, Japan). The dyes were then mixed with either 2 μL of αSyn, 5 μL of K18 tau (380 μg/mL), or 5 μL of $A\beta_{42}$ fibril (80 μg/mL) solution in a 45 μL Quartz SUPRASIL Ultra Micro Cell Cuvette (Hellma GmbH, Germany). The solutions were incubated for 1 min at room temperature and resuspended, and fluorescence was measured with a FluoroMax-4 spectrofluorometer (Horiba Jobin Yvon, Japan) using a known excitation wavelength for the ligands.

2.5 | In vivo and ex vivo imaging with the hybrid epiFL and vMSOT system

Concurrent epiFL imaging and vMSOT at pre-, during, and post-intravenous bolus injection of THK-565 were performed using a previously established hybrid system consisting of an epiFL fiberscope and a vMSOT

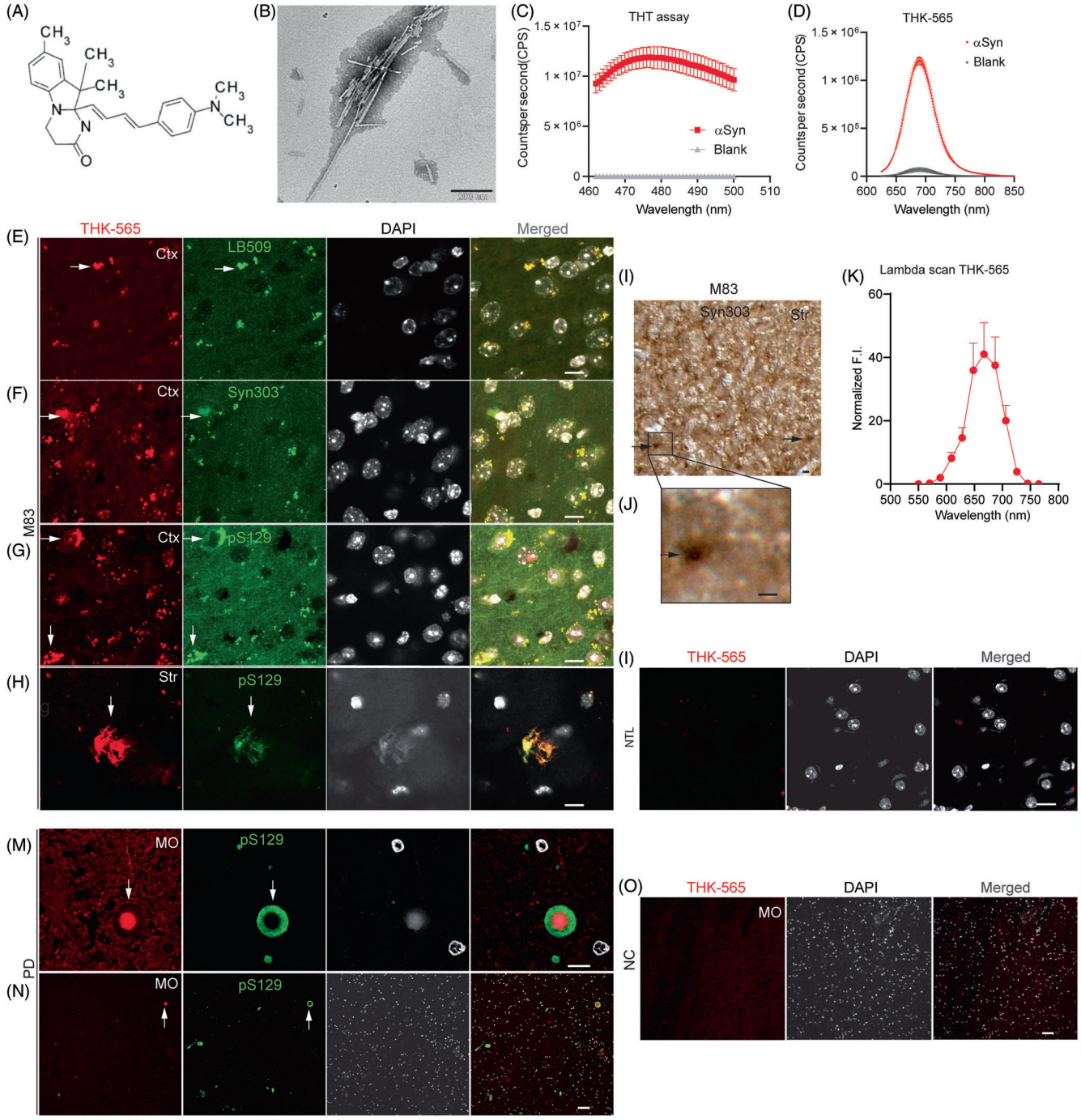

FIGURE 1 Characterization of THK-565 in recombinant alpha-synuclein (αSyn) fibrils, M83 mouse brains, and *post-mortem* Parkinson's disease (PD) and non-demented control brains. (A) Chemical structure of THK-565; (B) Transmission electron microscopy characterization of recombinant αSyn fibril; scale bar = 200 nm; (C) Thioflavin T assay of recombinant αSyn (red) fibril and blank (gray); (D) Spectrofluorometric measurements of the binding of THK-565 to recombinant αSyn (red) fibril and blank (gray); (E–H) Immunofluorescence staining using THK-565 (red), with anti-αSyn antibodies LB509, Syn303, and anti-p-αSyn antibody pS129 (green) on the cortex (Ctx) and striatum (Str) of the M83 mouse brain. (I, J) Immunocytochemistry using Syn303 antibodies on the M83 mouse Str; the arrow indicates αSyn inclusions. (K) Lambda scan of THK-565-stained αSyn inclusions in the M83 mouse brain. (L) Staining using THK-565 (red) on the striatum of nontransgenic littermate mouse brain. (M–O) Immunofluorescence staining using THK-565 (red), with pS129 (green) on the medulla oblongata of *post-mortem* tissue from a patient with PD (M, N); and non-demented control (O). Nuclei were counterstained using diamidino-2-phenylindole (DAPI) (gray). Scale bar = 10 μm (E–J, L, M); 50 μm (N, O).

imager [45]. The field-of-view (FOV) has a diameter of 12 mm for epiFL imaging and a volume of $15 \times 15 \times 15$ mm^3 for vMSOT, hence covering the entire mouse brain. The spatial resolution is approximately 40 and 120 μm for epiFL and vMSOT, respectively. Mice were first anaesthetized with an initial dose of 4%–5%

isoflurane (Abbott, Cham, Switzerland) in an oxygen/air mixture (200/800 mL/min) and subsequently maintained at 1.5% isoflurane in oxygen/air (100/400 mL/min) throughout the measurement. The fur over the head of the mice was removed before they were placed in the prone position on a heating pad with feedback control to maintain a constant body temperature (PhysioSuit, Kent Scientific, USA). The mice were subsequently injected with a 10 μL bolus containing THK-565 (Figure 1A), dissolved in DMSO, 0.1 M PBS, pH 7.4, followed by 90 μL saline through the tail vein. A dose of 20 mg/kg body weight was chosen and used in the following experiment. For vMSOT, the pulse repetition frequency of the laser was set to 25 Hz, and the laser wavelength was tuned between 550 and 660 nm (5 nm step) on a per pulse basis. epiFL imaging was performed by coupling the same beam from the pulsed optical parametric oscillator (OPO) laser into the excitation fiber bundle. The excited fluorescence signal was collected by an imaging fiber bundle comprised of 100,000 fibers and then projected onto an electron multiplying charge-coupled device camera (Andor iXon Life 888, Oxford Instruments, UK). Dynamic signals from epiFL and vMSOT were recorded simultaneously and synchronized with an external device (Pulse Pal V2, Sanworks, USA). To determine the optimal imaging time window, one mouse was scanned every 30 min starting at 60 min post-injection of THK-565 until 320 min after the injection of THK-565. For the remaining mice, the scan time points were before injection (108 s duration), during injection (432 s duration with intravenous injection starting at 30 s after the beginning of acquisition), and 20, 40, 60, and 90 min post-injection (108 s duration each).

The reconstructed vMSOT images were spectrally processed to unmix the biodistribution of THK-565. For this, either per-voxel least square fitting of the spectral signal profiles to a linear combination of the absorption spectra of HbO_2 and THK-565 was performed [33, 45, 46], or the baseline (image taken prior to THK-565 injection) was subtracted from the vMSOT images at 635 nm. Given that there is no brain atrophy in the mice (based on ex vivo MRI data described below), the resulting images were coregistered with a structural MRI atlas (Ma-Benveniste-Mirrione-T_2) in PMOD 4.2 (Bruker, Germany) for volume-of-interest (VOI)-based data analysis (Bruker, Germany). The fluorescence and vMSOT signal intensity were adjusted by dose/weight and normalized to a 0–1 scale.

2.6 | Ex vivo MRI of M83 mouse brains

M83 and NTLs were intracardially perfused under deep anesthesia (ketamine/xylazine/acepromazine maleate; 75/10/2 mg/kg body weight, i.p. bolus injection), with 0.1 M PBS (pH 7.4), followed by 4% paraformaldehyde in 0.1 M PBS (pH 7.4). The heads were post-fixed in 4% paraformaldehyde in 0.1 M PBS (pH 7.4) for 6 days and stored in 0.1 M PBS (pH 7.4) at 4°C. Brains were not removed from the skull, which has been shown previously to preserve cortical and central brain structure. The heads were placed in a 15 mL centrifuge tube filled with perfluoropolyether (Fomblin Y, LVAC 16/6, average molecular weight 2700, Sigma-Aldrich, USA). MRI data were acquired on a BioSpec 94/30 with a cryogenic 2 × 2 radio frequency phased-array surface coil (overall coil size 20 × 27 mm^2, Bruker BioSpin AG, Fällanden, Switzerland) with a coil system operating at 30 K (Bruker BioSpin AG, Fällanden, Switzerland) for reception used in combination with a circularly polarized 86 mm volume resonator for transmission. For SWI, a global and MAPSHIM protocol with a field map (default settings) were used for shimming [47]. A 3D gradient-recalled echo SWI sequence was recorded with the following parameters: FOV = 15 × 12 × 15 mm; image size = 248 × 199 × 36 μm, resulting in a spatial resolution = 60 × 60 × 438 μm. One echo with a echo time = 12 ms; repetition time = 250 ms; flip angle = 15°; number of averages = 4, acquisition scan time = 1 h 59 min 24 s. SWI and phase images were computed using the SWI processing module in ParaVision 6.0.1 (Bruker, Ettlingen, Germany) with Gauss broadening = 1 mm and mask weighting = 4. All SWI images were compared with their phase image counterparts. MRI images were analyzed in ITK SNAP [48] and evaluated by two people blinded to the genotype of the mice.

2.7 | Ex vivo multiphoton microscopy, histology, immunofluorescence, and confocal imaging

We assessed the binding of THK-565 to αSyn inclusions in M83 mouse brains and *post-mortem* brain tissue from a patient with PD, as well as to Aβ plaques and tau inclusions in arcAβ and P301L mouse brains and *post-mortem* brain tissue from patients with AD, PSP, and CBD, by using immunofluorescence staining. Staining was performed on the brain tissue slices from the non-demented control case and NTL mouse brains to assess the specificity of the probe. For mouse brain samples, the brain was cut into 40 μm-thick coronal sections using a vibratome (Leica VT1000S, Germany) for free-floating immunofluorescence immunohistochemistry or embedded in paraffin following routine procedures and cut into 5 μm-thick sections for histology. For paraffin-embedded *post-mortem* human brain tissues, 5 μm-thick sections were cut for histopathology. Costaining was performed using ligands and anti-phospho-tau antibody AT-8, anti-Aβ antibody 6E10, anti-αSyn antibodies LB509 (total αSyn), Syn303 (oxidized αSyn), and pS129 (phosphorylated αSyn), as described earlier (details in Table S1) [44, 49]. Counterstaining was performed using 4′,6-diamidino-2-phenylindole (DAPI).

To validate the uptake of THK-565 inside the brain of the M83 mouse and assess the signal/noise ratio, we performed ex vivo multiphoton microscopy at 10× and 20× magnification using a Leica TCS SP8 Multiphoton microscope (Leica, Germany). Coronal brain slices (40 µm-thick) from the fixed brain of the M83 mouse after 320 min injection of THK-565 (intravenous) and the whole frozen brain of another M83 mouse after 120 min injection of THK-565 (in vivo) were imaged. Lambda scan was acquired, and the images were analyzed.

Hematoxylin & eosin (H&E) staining and Prussian blue (for iron deposit detection) staining were performed in M83 mouse brains. Brain sections were imaged at 20× magnification using an Axio Oberver Z1 and at 63× magnification using a Leica SP8 confocal microscope (Leica, Germany) for colocalization evaluations. A lambda scan using a Leica SP8 was performed on stained brain slices to further determine the fluorescent properties of THK-565. The images were analyzed using Qupath and ImageJ (NIH, USA).

2.8 | Scanning transmission x-ray microscopy

x-Ray spectromicroscopy (scanning transmission x-ray microscopy [STXM]) was performed at the Swiss Light Source (SLS, PSI, Switzerland) at the PolLux beamline (X07DA) [50]. Samples were prepared by cutting adjacent brain sections, of which Prussian blue staining was performed, into 60 nm thin sections and placing them on a copper electron microscopy grid. The samples were raster-scanned across an x-ray beam focused by a Fresnel zone plate with an outermost zone width of 35 nm, setting the spatial resolution limit of the measurement to about 50 nm. The transmitted x-ray beam was detected by a scintillator coupled to a photomultiplier tube. To map the distribution of iron, paired images were taken below (705 eV) and above (730 eV) the Fe $L_{2,3}$ edge, and candidate objects were further investigated with a spectrum at the Fe $L_{2,3}$ edge.

2.9 | Statistics

Group comparison of THK-565 absorbance in multiple brain regions at different time points was performed by using a two-way analysis of variance (ANOVA) with Bonferroni post hoc analysis using GraphPad Prism 9 (GraphPad, USA). The difference in the fluorescence intensity acquired by epiFL imaging at different time points was compared using a one-way ANOVA. All data are presented as the mean ± standard deviation. Pearson's rank correlation analysis was used to compare vMSOT and epiFL imaging data and reliability analysis. Significance was set at $*p < 0.05$.

3 | RESULTS

3.1 | Detection of αSyn recombinant fibrils and αSyn inclusions in mouse and human brain slices

First, we produced $A\beta_{42}$, K18 tau, and αSyn fibrils using bacterially produced recombinant monomers and validated them using the Thiovlavin T assay and transmission electron microscopy (TEM, Figures 1B,C and S1a,b,d,e). THK-565 showed increased fluorescence emission in the presence of $A\beta_{42}$, K18 tau, and αSyn fibrils (Figures 1D and S1c,f). The emission spectrum of THK-565 did not differ among the $A\beta_{42}$, K18 tau, and αSyn fibrils tested. THK-565 showed suitable absorbance and emission spectra for in vivo vMSOT.

Immunofluorescence staining of M83 mouse brain slices showed colocalization of the THK-565 signal with LB509-positive, Syn303-positive, and pS129-positive αSyn inclusions (Figure 1E–H). Immunocytochemistry using Syn303 antibodies further validated the presence of αSyn inclusions (Figure 1I,J). A lambda scan of THK-565-stained αSyn inclusions in the M83 mouse brain indicated that the peak of the emission spectrum was similar to that obtained from αSyn fibrils (Figure 1K). In the striatum tissue slice of one NTL, THK-565 did not show any specific signal (Figure 1L).

Immunofluorescence staining of medulla oblongata brain tissue from a PD patient showed detection of THK-565 in the core part of pS129-positive αSyn intraneural inclusions, Lewy bodies, and Lewy neurites (Figure 1M,N). In the medulla oblongata tissue of one non-demented control absent of αSyn (LB Braak 0), THK-565 did not show any specific signal (Figure 1O).

In addition, we observed that THK-565 also stained 6E10-positive amyloid-beta plaques in the arcAβ mouse brain and AT-8-positive tau inclusions in the pR5 mouse brain (Figure S2a,b). A lambda scan of THK-565-stained Aβ plaques and tau inclusions (Figure S2c,d) in the mouse brain indicated that the peak of the emission spectrum was similar to that from M83 mice (Figure 1K).

However, at the same concentration (10 µM), THK-565 stained weakly the AT-8-positive "tufted" astrocytic tau inclusions in the putamen/pallidum with insula from the PSP brain or the neuronal tau inclusion or neurites in the caudate/putamen from CBD cases (Figure S3a,b). These staining indicate that there might be a difference in the binding affinity of amyloid and tau compared to αSyn in the human brain. The pattern of THK-565 to the 6E10-positive Aβ deposits and AT-8 positive tau deposits in the human brain was also different from that in the mouse brain, probably because of a difference in the structure of Aβ and tau deposits in the human and mouse brains.

3.2 | Noninvasive in vivo vMSOT and epiFL of THK-565 uptake in the M83 mouse brain

The vMSOT imaging data analysis pipeline consisted of three steps: 3D vMSOT image reconstruction, isolation of the specific THK-565 signal via spectral unmixing or baseline subtraction, and coregistration with an MRI mouse brain atlas for VOI analysis, as described earlier [45, 51]. After intravenous bolus injection of THK-565, an increase in the fluorescence intensity and spectrally unmixed THK-565 signal was observed in the mouse brain parenchyma, indicating passage through the BBB. Albeit lacking depth information, the THK-565 epiFL images of the brain corroborated the corresponding increase in the vMOST signal associated with optical absorption by THK-565 (Figure 2A–D). To determine the optimal imaging time frame, we imaged one M83 mouse for 320 min post-injection of THK-565 and the rest of the mice for 90 min post-injection. Given that the approved in vivo imaging experiment was terminal, we did not keep the animal for imaging at 24 or 48 h post-injection. The wavelengths and absorbing components were optimized so that the unmixed biodistribution of THK-565 matched the differential vMSOT images (ΔvMSOT) taken at 635 nm after subtracting a reference image obtained before injection. A clear increase/peak in the vMSOT and fluorescence signal intensity was observed upon injection, which was used for retrieving the THK-565 absorption spectrum and the subsequent unmixing analysis (Figure 2E). We used five wavelengths (600, 610, 620, 630, and 635 nm) during unmixing and only HbO_2 and THK-565 as absorbing components (Figure 2F). We observed that both the fluorescence and vMSOT signals were stable at 60–90 min post-injection (Figure 2E–J). The spectrally unmixed THK-565 appeared to have less agreement with the fluorescence dynamics compared with the ΔvMSOT data at 635 nm (Figure 2J). The apparent lack of accuracy of multispectral unmixing is ascribed to strong changes in hemoglobin absorption with wavelength, leading to so-called spectral coloring effects [52]. A strong correlation between ΔvMSOT and fluorescence intensity was observed (Figure S4, $p < 0.0001$, $r = 0.9562$, Pearson's rank correlation analysis). Therefore, we used a 90 min imaging frame (20, 40, 60, and 90 min) in the subsequent in vivo epiFL-vMSOT experiments and relied on the ΔvMSOT signal at 635 nm for quantification [32]. To assess the stability of the fluorescence and vMSOT signal, we imaged one mouse without intravenous injection of contrast agent for 90 min. No alterations in the fluorescence, unmixed or differential vMSOT signal intensity over the whole-brain region were observed (Figure 2K–M).

To validate the uptake of THK-565 in the brain and to assess its signal and noise in the brain of mouse, we imaged two brains from M83 mice after in vivo imaging using ex vivo multiphoton. Specific fluorescence signals was detected in the cortex and striatum of the coronal brain slice from one M83 mouse after a 320 min injection of THK-565 (intravenous) and in the cortical surface of the frozen whole brain (without fixation) from one M83 mouse after a 120 min injection of THK-565 (i.v) (Figure S5). Lambda scan performed on the cortex and striatum of the frozen brain section indicated the emission spectrum of THK-565 in the tissue from the M83 mouse after 320 min intravenous injection and imaging.

3.3 | THK-565 biodistribution in M83 and NTL mouse brains

M83 and NTL mice were imaged before, during, and after injection of THK-565 (20 mg/kg weight, i.v.) using the concurrent epiFL-vMSOT system. Higher fluorescence intensity (635 nm excitation) was observed in the brains of M83 mice than in those of NTL mice (Figure 3A). Significantly higher percentile changes in fluorescence intensity (635 nm excitation) were observed in the whole brains of M83 mice than in those of NTL mice ($p = 0.0048$, Figure 3B,C). The vMSOT images acquired at a wavelength of 635 nm were superimposed onto the MRI atlas for VOI analysis (Figure 3D,E). No significant changes in the differential ΔvMSOT signal corresponding to THK-565 in specific brain regions of M83 and NTL mice were observed (Figure 3F,G).

3.4 | SWI/phase and STXM imaging detect iron deposits

SWI sequences have been used to evaluate iron deposits in the brain. Ex vivo studies of the mouse brain using 9.4 T MRI and a cryogenic radiofrequency coil helped achieve high signal-to-noise ratios. To differentiate whether paramagnetic or diamagnetic lesions were present, a phase image was reconstructed. Iron is a ferromagnetic material and appears as black dots on both SWI and phase images. We found hypointensities in the SWI images and negative phase shifts indicative of iron in the striatum of M83 mice (Figure 4A). An earlier study showed that ferrous and ferric iron ions show significantly different relaxation behaviors in MRI but similar susceptibility patterns [53]. Therefore, to further understand the distributions and properties of iron species, we performed STXM on the striatum part of the brain tissue section with paired images taken at 705 and 730 eV to identify Fe-rich deposits. Based on the Fe $L_{2,3}$-edge NEXAFS spectrum measurements on the identified deposits, we concluded that Fe^{3+} deposits were detected in the striatum of the M83 mouse brain (Figure 4B,D). Next, we validated the presence of iron by using Prussian blue staining on the adjacent slides. Blue spots in the striatum and cortex were observed in the M83 mouse brain from Prussian blue staining, indicative of the presence of iron deposits (Figure 4C).

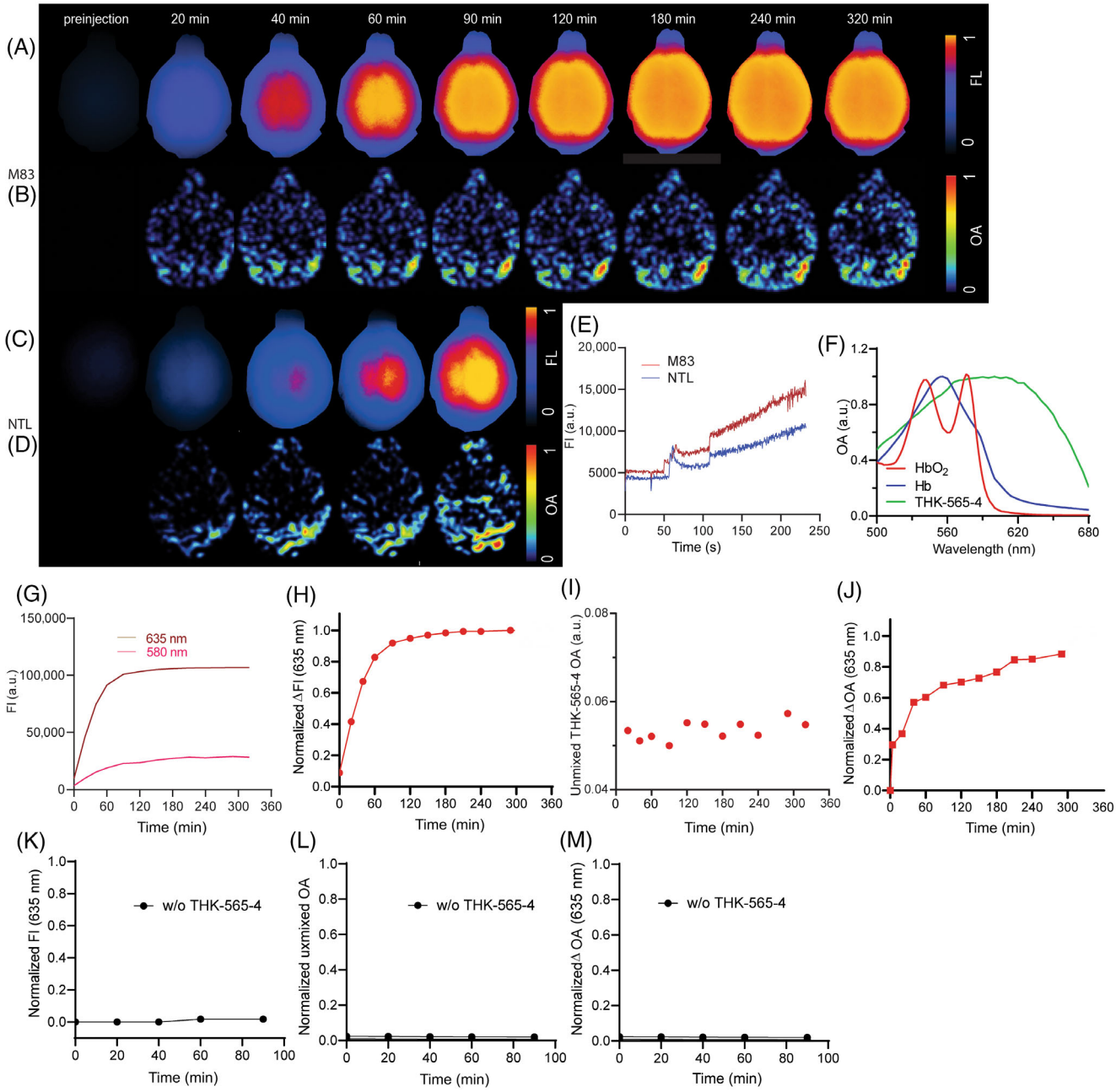

FIGURE 2 In vivo concurrent epifluorescence (epiFL) and volumetric multispectral optoacoustic tomography (vMSOT) using THK-565. (A–D) Representative normalized epiFL and vMSOT images at different time points from preinjection of THK-565 until 320 min post-injection in the brain of one M83 mouse (A, B), and until 90 min post-injection in the brain of one nontransgenic littermate (NTL) mouse (C, D) (horizontal view). (E) The time difference in the normalized vMSOT signal during the injection of THK-565 was used to distinguish THK-565 from oxy-/deoxyhemoglobin (HbO_2/Hb) and background. (F) Absorbance spectrum of THK-565 (retrieved from the in vivo vMSOT data) and HbO_2/Hb [46]. (G, H) Quantification of absolute fluorescence intensity (FI) at 580 and 635 nm excitation, normalized differential FI at 635 nm, (I, J) Quantification of unmixed THK-565 optoacoustic (OA) intensity, and normalized ΔvMSOT intensity over the whole brain of M83 mice after THK-565 intravenous injection. (K–M) Stable normalized FI, ΔvMSOT, and unmixed ΔvMSOT over 90 min in the brain of one M83 mouse without THK-565 injection. ΔvMSOT = ΔOA.

3.5 | SWI and phase imaging detect diamagnetic lesions

Calcium is a paramagnetic material, such that abnormal calcium deposits will be imaged as black dots on the SWI image (combining filtered magnitude and phase data) but as white dots on the phase image. In addition to the iron deposits, we observed hypointensities in the SWI images and positive phase shifts indicative of calcification in the brains of M83 mice by ex vivo MRI (Figure 5A). The hypointensities were observed in the hippocampus, striatum, and thalamus, as well as in the midbrain. Next

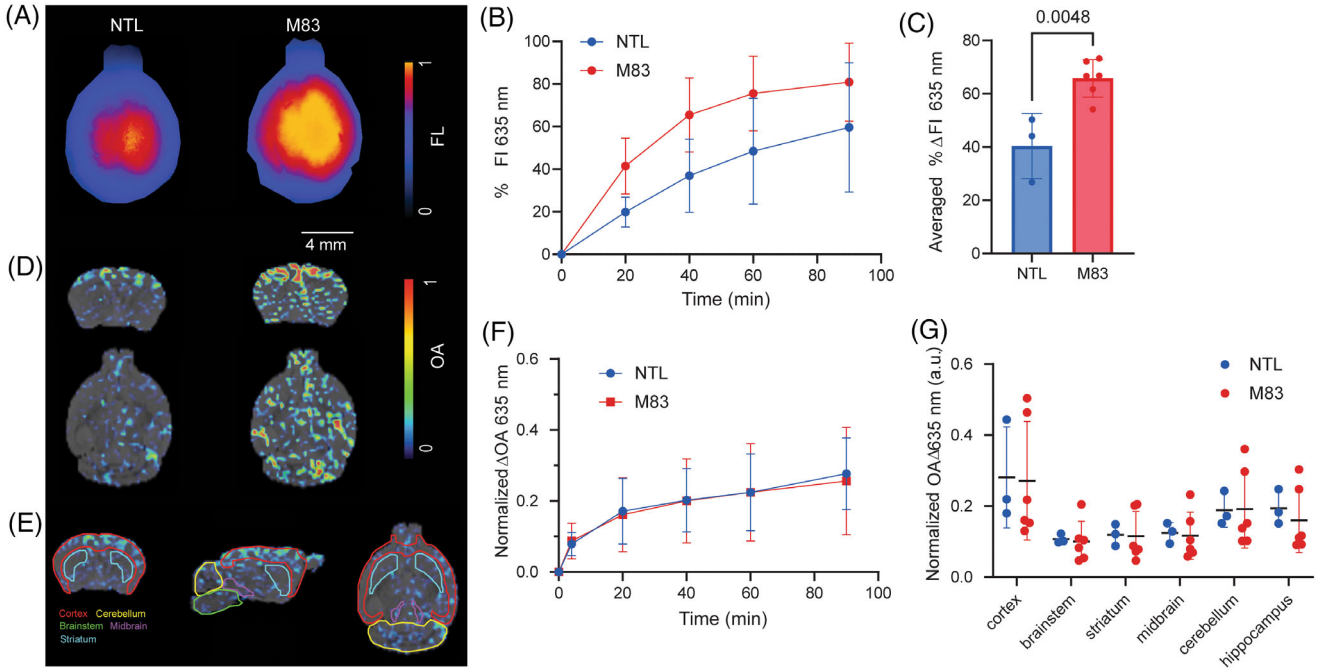

FIGURE 3 Increased THK-565 uptake in the brains of M83 mice compared to nontransgenic littermate (NTL) mice. (A) Representative epifluorescence images of NTL and M83 mouse brains at 40 min post-THK-565 intravenous injection. (B) Percent increase in fluorescence intensity over 90 min in the brains of M83 and NTL mice after THK-565 intravenous injection. (C) Percent increase in fluorescence intensity in the brains of M83 compared to those of NTL mice. (D) Representative THK-565 signal resolved by volumetric multispectral optoacoustic tomography (vMSOT) at 40 min post-THK-565 intravenous injection (coronal and horizontal view). (E) Mouse brain atlas overlaid on the vMSOT images of the mouse brain (coronal, sagittal, and horizontal view). (F) Whole-brain normalized ΔvMSOT signal intensity over 90 min in M83 and NTL mice after THK-565 intravenous injection. (G) Regional analysis of the normalized ΔvMSOT signal at 20–40 min post-HK-565 intravenous injection. ΔvMSOT = ΔOA. FI, fluorescence intensity.

we validated the presence of calcification by using H&E staining. Blue-stained deposits in the cerebellum of the M83 mouse brain were observed (Figure 5B).

4 | DISCUSSION

New tools for noninvasive mapping of αSyn and iron deposits with high resolution facilitate understanding of disease mechanisms and the development of therapeutics [54]. Herein, we visualized the in vivo αSyn distribution in the brain of the M83 mouse model using a hybrid epiFL-vMSOT system assisted by a targeted THK-565 fluorescent label. The presence of iron deposits (presumably Fe^{3+}) was further demonstrated by using high-field SWI MRI and STXM in the striatum and cortex of M83 mice ex vivo.

Here we used different αSyn antibodies to verify and characterize the binding of THK-565 on αSyn deposits. We used pS129 that bound to pathological αSyn phosphorylated on the Ser129 epitope, Syn303 that binds a pathological conformation of oxidized/nitrated αSyn on N-terminal (amino acids 1–5) epitope. In addition, we used LB509, which bound to all αSyn forms (mono, oligo, and fibrils on the C-terminal [amino acids 115–122]) epitope. THK-565 binds to the beta-sheet structure of the αSyn aggregates (not to monomer) and is not able to differentiate different epitopes of αSyn as a chemical probe. It is noted that THK-565 binds to the core (Figure 1M,N), whereas pS129 binds to the rim of αSyn deposits in the PD brain slice. The reason for this is not fully clear. It is possible that chemical probes have better penetration. This pattern was observed by using other beta-sheet binding chemical probes such as luminescent conjugated oligothiophene HS-169 in our other study involving staining of αSyn deposits in PD human brain tissue [44]. It is not clear whether THK-565 can bind to oligomeric or prefibrillar forms of αSyn aggregates, as these are difficult to detect, and whether the binding can reflect toxic type of αSyn aggregates.

M83 mice show signs of motor impairment from 8 months of age. The presentation of this phenotype is associated with the formation of αSyn inclusion pathology throughout most of the spinal cord and brainstem. αSyn deposits start at 5 months of age and develop accumulations of αSyn in select neuronal populations, including the midbrain, cerebellum, brainstem, cortex, and spinal cord [35]. The protein aggregates do not resemble Lewy bodies but are thioflavin-S-positive, indicating a fibrillar structure [35]. THK-565 facilitated sensitive detection of αSyn fibrils and inclusion slices of transgenic M83 mice and human PD brains. THK-565 was selected

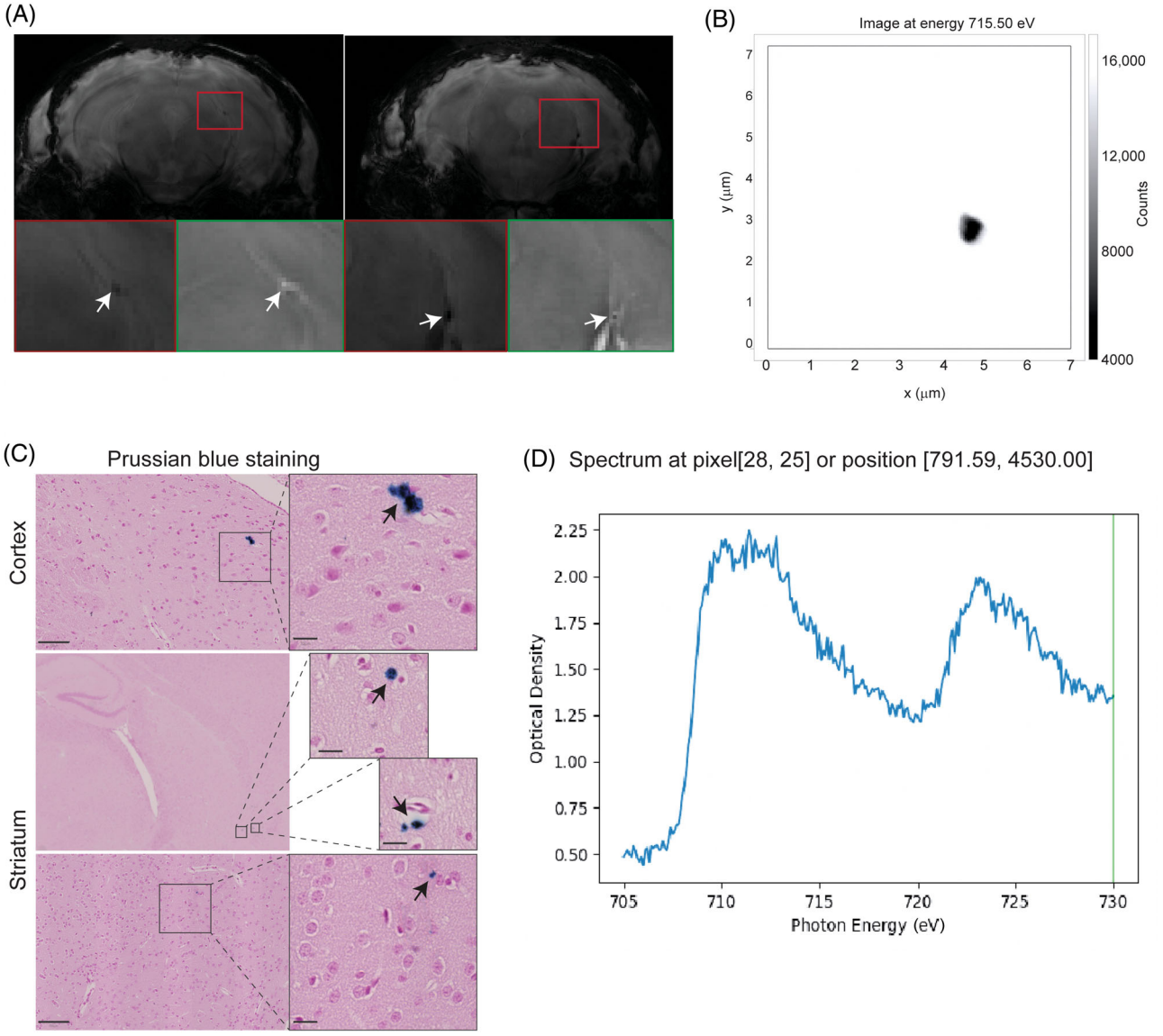

FIGURE 4 Imaging evidence of intracranial iron deposition in the M83 mouse. (A) Ex vivo SWI at 9.4 T and corresponding phase image showing hypointensities/negative phase shifts indicating paramagnetic iron deposition in the M83 mouse brain (indicated by arrow). (B) Scanning transmission x-ray microscopy showed iron-rich deposits in the striatum of the adjacent brain slice of the Prussian blue-stained slice. (C) Prussian blue staining indicating the presence of iron deposition in the cortex and striatum of the M83 mouse brain. (D) Optical density of Fe $L_{2,3}$-edge spectrum of the deposit indicates that the iron species is Fe^{3+}.

because of its peak absorption at 635 nm, where light penetration is significantly enhanced with respect to shorter wavelengths. In this way, THK-565 could be more clearly distinguished from endogenous chromophores such as Hb and HbO_2 via spectral unmixing of vMSOT images acquired in vivo. The cortical and striatal signals detected by vMSOT in vivo and ex vivo using THK-565 are in accordance with the immunofluorescence staining results and with the reported αSyn distribution in the M83 mouse brain [35]. However, the detection sensitivity of vMSOT appeared lower than that of concurrent fluorescence recordings, which demonstrated a sufficient difference in the signal intensity between M83 and NTL mice. The lack of difference in the vMSOT signal is partly because of the large background signal fluctuations (because of the pulsed laser instability) as well as the relatively low amount of αSyn inclusions in M83 mice at 10–11 months of age. Follow-up studies may focus on the exploration of brains from 18 months that have a higher load of aSyn fibrils that were not permitted in the current animal experimentation approval.

Near-infrared fluorescence imaging detection in deep brain regions was hindered by the strong absorption and scattering of the excitation light and emitted fluorescence. Submillimeter-scale intravital and multiphoton

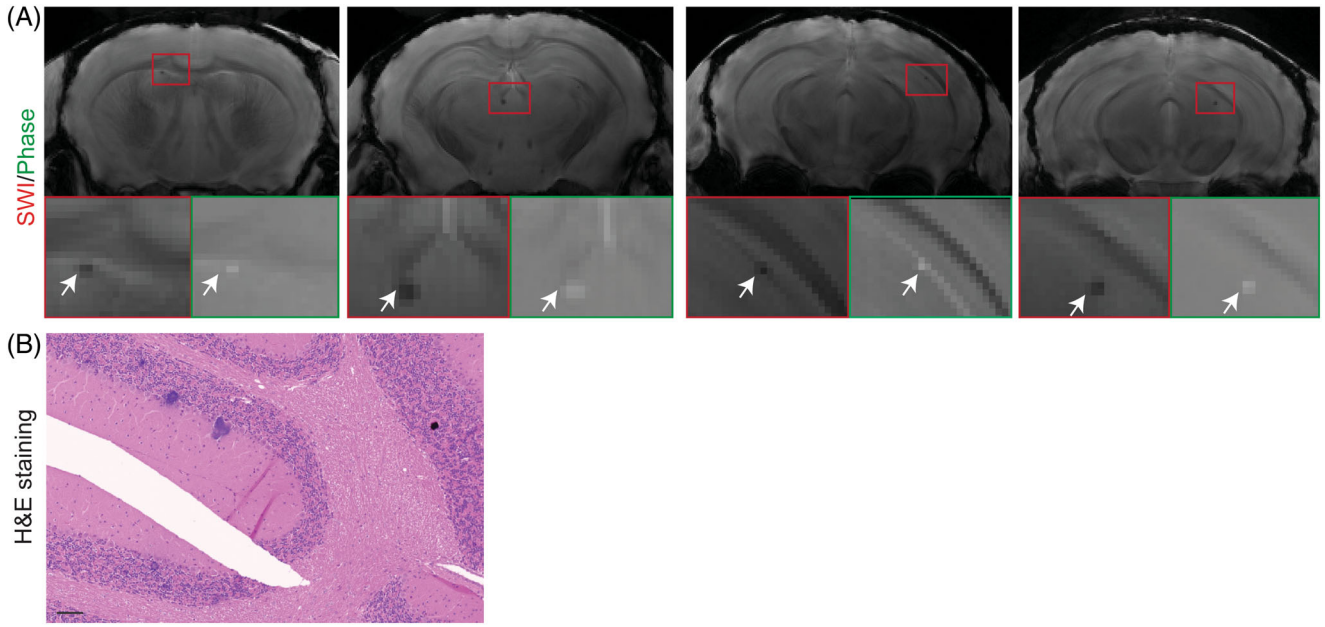

FIGURE 5 Susceptibility weighted imaging (SWI) and phase imaging reveal intracranial calcification in the M83 mouse. (A) Ex vivo SWI magnetic resonance imaging at 9.4 T and corresponding phase image showing hypointensities/positive phase shifts indicting diamagnetic calcification in the M83 mouse brain, including striatum, thalamus, hippocampus, and midbrain (indicated by arrow) (B) Hematoxylin & eosin staining indicate the presence of calcification in the cerebellum of the mouse brain.

microscopies enable the visualization of αSyn deposits mainly in the cortex but are highly invasive and can only cover a very limited FOV [55–57]. Spectral unmixing can generally isolate the biodistribution of any spectrally distinctive probe from endogenous absorbers in biological tissues. However, spectral coloring effects associated with wavelength-dependent attenuation of light lead to crosstalk artifacts when considering the theoretical spectra of the absorbing substances present in the sample [52]. This is particularly important for wavelengths exhibiting sharp variations in HbO_2 absorption, for example, the 605–635 nm spectral range [46]. However, reliable fluence correction is still an unsolved problem; thus, we opt not to apply complex processing [58].

Brain iron deposition is linked with dopamine, neuromelanin pathways, and cognitive severity in PD [59–61]. Brain iron enrichment attenuates αSyn spreading after injection of preformed fibrils [62]. *Mutations in LRRK2 linked to PD sequester Rab8a to damaged lysosomes and regulate transferrin-mediated iron uptake in microglia* [63]. A few MRI studies have been performed in animal models of PD, such as using T_2* [5, 6, 64], as well as in patients with PD using novel MRI contrasts, SWI, QSM, and R_2 R_2* [7, 8, 10, 65–70]. A previous study using 3D elemental bioimaging showed Fe, Zn, Cu, Mn, and P in a 6-hydroxydopamine-lesioned mouse brain [71, 72]. Here, we demonstrated regional hypointensities in the hippocampus, cortex, striatum, midbrain, and thalamus by using SWI images of M83 mice, which in corresponding phase images indicated paramagnetic (iron) lesions in the brains of M83 mice. Moreover, the STXM detection of Fe^{3+} deposits in the adjacent slice of Prussian blue-stained iron deposits in the striatum further validated this finding. The striatum is a vulnerable brain region that loses its dopaminergic innervation and is affected early in PD patients and transgenic animal models of PD [73]. The striatum and cortex of the M83 mouse thus bear both αSyn inclusions and iron deposits. In addition, we also observed calcification in the M83 mouse brain by SW/phase MR. Basal ganglia calcifications [74] have been reported in patients with PD [75].

There are several limitations to the current study. Additional longitudinal study is required to determine the actual sensitivity and specificity of the proposed methodology, namely, the age of M83 mice in which THK-565-positive αSyn inclusions can be detected by vMSOT, and whether it can follow the spreading of αSyn in the brain. Given the relatively low load of αSyn inclusions in the transgenic animal model at this age, αSyn preformed fibril-injected animals or AAV-αSyn models might have an advantage in the assessment of αSyn imaging tracers with the possibility of a high load of αSyn inclusion in the brain. On the other hand, later disease stages at 18–24 months of age in M83 mice also shed light on the ability of these methodologies to monitor disease progression. Such studies in aged M83 mice were limited by a lack of local veterinary approval because of phenotypic constraints. It is noted that THK-565 detects Aβ, tau in addition to αSyn, which limits its value in differentiating different aggregates. In addition, differences in the detection pattern of THK-565 are observed in the brain tissue samples from PSP, CBD human patients,

and mouse models of tauopathy. Further studies are needed to understand the binding pocket and mechanism of THK-565 to different amyloid fibrils.

In conclusion, we demonstrated successful noninvasive imaging of αSyn in M83 mice with a concurrent epiFL-vMSOT system at high spatial resolution and volumetric coverage of the brain. This in vivo imaging platform provides a new tool to map αSyn distribution in αSyn mouse models, which may facilitate the monitoring of αSyn-targeting therapeutics.

AUTHOR CONTRIBUTIONS

The study was designed by RN. NO provided THK-565. JAG performed recombinant fibril production and binding measurements. ZC, XLDB and DR designed and built the hybrid fluorescence and vMSOT system. RN performed in vivo imaging and XLDB, NS operated the MSOT system. ID and DN performed animal breeding and genotyping, MHL and RN performed ex vivo MRI. RS-H, JL, BW, and IR performed thin sample preparation and scanning x-ray microscopy. BFC and DN performed histology and confocal microscopy. JKW (ScopeM) performed ex vivo multiphoton microscopy. NS, BFC, XLDB, and RN performed the data analysis. NS, BFC, DN, JAG, XLDB, NO, DR, and RN interpreted the data. RMN, KS, and AR provided infrastructure. RN wrote the first draft. All authors contributed to the revision of the manuscript. All the authors have read and approved the final manuscript.

ACKNOWLEDGMENTS

The authors acknowledge Dr. Saroj Kumar Rout at ETH Zurich, Mr. Michael Reiss, Prof. Jan Klohs, and Ms. Agathe Tournant at the Institute for Biomedical Engineering, Dr. Justin Kusch-Wiser, ScopeM, ETH Zurich/University of Zurich, Ms Man Hoi Law at Imperial Colleague London; Mr Vasil Kecheliev, Mr Daniel Schuppli at the Institute for Regenerative Medicine, University of Zurich; and ZMB for technical assistance. We acknowledge the Paul Scherrer Institute, Villigen, Switzerland for provision of synchrotron radiation beamtime at the PolLux beamline of the SLS. The PolLux end station was financed by the German Ministerium für Bildung und Forschung (BMBF) through contracts 05K16WED and 05K19WE2.

FUNDING INFORMATION

Ruiqing Ni received funding from Novartis Foundation for Medical-Biological Research, Olga Mayenfisch Stiftung, Swiss Center for Applied Human Toxicology (AP22-02), and Fondation Gustave et Simone Prévot. Daniel Razansky acknowledges grant support from the Swiss National Science Foundation (310030_192757), US National Institutes of Health (R01-NS126102-01). Ruiqing Ni and Daniel Razansky acknowledge support from the Swiss National Science Foundation (31ND30_213444). Ruiqing Ni, Xose Luis Dean Ben, and Daniel Razansky acknowledge support from Innosuisse (51767.1 IP-LS). Ines Dias and Daniela Noain received funding from Parkinson Schweiz, and Daniela Noain received funding from the Dementia Research Switzerland-Foundation Synapsis (2018PI-03).

CONFLICT OF INTEREST STATEMENT

Roger M. Nitsch is an employee and shareholder of Neurimmune AG. Other authors declare no conflicts of interest.

DATA AVAILABILITY STATEMENT

All raw data are available upon request to corresponding author.

ETHICS STATEMENT

All experiments were performed in accordance with the Swiss Federal Act on Animal Protection and were approved by the Cantonal Veterinary Office Zurich (license numbers: ZH024/21, ZH162/20). All human brain tissue materials had been collected from donors or from whom written informed consent for a brain autopsy and the use of the materials and clinical information for research purposes by NBB, Netherlands. The study was conducted according to the principles of the Declaration of Helsinki and subsequent revisions. All experiments on autopsied human brain tissue were carried out in accordance with ethical permission obtained from the regional human ethics committee in Canton Zurich and the medical ethics committee of the VU Medical Center for the NBB tissue.

ORCID

Ruiqing Ni https://orcid.org/0000-0002-0793-2113

REFERENCES

1. Politis M. Neuroimaging in Parkinson disease: from research setting to clinical practice. Nat Rev Neurol. 2014;10(12):708–22.
2. Höglinger GU, Adler CH, Berg D, Klein C, Outeiro TF, Poewe W, et al. A biological classification of Parkinson's disease: the SynNeurGe research diagnostic criteria. Lancet Neurol. 2024; 23(2):191–204.
3. Simuni T, Chahine LM, Poston K, Brumm M, Buracchio T, Campbell M, et al. A biological definition of neuronal α-synuclein disease: towards an integrated staging system for research. Lancet Neurol. 2024;23(2):178–90.
4. Yu H, Guo P, Xie X, Wang Y, Chen G. Ferroptosis, a new form of cell death, and its relationships with tumourous diseases. J Cell Mol Med. 2017;21(4):648–57.
5. Do TM, Alata W, Dodacki A, Traversy MT, Chacun H, Pradier L, et al. Altered cerebral vascular volumes and solute transport at the blood-brain barriers of two transgenic mouse models of Alzheimer's disease. Neuropharmacology. 2014;81: 311–7.
6. Virel A, Faergemann E, Orädd G, Strömberg I. Magnetic resonance imaging (MRI) to study striatal iron accumulation in a rat model of Parkinson's disease. PLoS One. 2014;9(11):e112941.
7. Acosta-Cabronero J, Cardenas-Blanco A, Betts MJ, Butryn M, Valdes-Herrera JP, Galazky I, et al. The whole-brain pattern of magnetic susceptibility perturbations in Parkinson's disease. Brain. 2017;140(1):118–31.

8. Lotfipour AK, Wharton S, Schwarz ST, Gontu V, Schäfer A, Peters AM, et al. High resolution magnetic susceptibility mapping of the substantia nigra in Parkinson's disease. J Magn Reson Imaging. 2012;35(1):48–55.
9. Lee JH, Lee MS. Brain iron accumulation in atypical parkinsonian syndromes: in vivo MRI evidences for distinctive patterns. Front Neurol. 2019;10:74.
10. Jin L, Wang J, Zhao L, Jin H, Fei G, Zhang Y, et al. Decreased serum ceruloplasmin levels characteristically aggravate nigral iron deposition in Parkinson's disease. Brain. 2011;134(Pt 1):50–8.
11. Ayton S, Lei P, Adlard PA, Volitakis I, Cherny RA, Bush AI, et al. Iron accumulation confers neurotoxicity to a vulnerable population of nigral neurons: implications for Parkinson's disease. Mol Neurodegener. 2014;9:27.
12. Imam SZ, Lantz-McPeak SM, Cuevas E, Rosas-Hernandez H, Liachenko S, Zhang Y, et al. Iron oxide nanoparticles induce dopaminergic damage: in vitro pathways and in vivo imaging reveals mechanism of neuronal damage. Mol Neurobiol. 2015; 52(2):913–26.
13. Angelova PR, Choi ML, Berezhnov AV, Horrocks MH, Hughes CD, De S, et al. Alpha synuclein aggregation drives ferroptosis: an interplay of iron, calcium and lipid peroxidation. Cell Death Differ. 2020;27(10):2781–96.
14. Ortega R, Carmona A, Roudeau S, Perrin L, Dučić T, Carboni E, et al. α-Synuclein over-expression induces increased iron accumulation and redistribution in iron-exposed neurons. Mol Neurobiol. 2016;53(3):1925–34.
15. Ni R. PET imaging in animal models of Parkinson's disease. Behav Brain Res. 2022;438:114174.
16. Kuebler L, Buss S, Leonov A, Ryazanov S, Schmidt F, Maurer A, et al. [(11)C]MODAG-001-towards a PET tracer targeting α-synuclein aggregates. Eur J Nucl Med Mol Imaging. 2021;48(6): 1759–72.
17. Morito T, Harada R, Iwata R, Du Y, Okamura N, Kudo Y, et al. Synthesis and pharmacokinetic characterisation of a fluorine-18 labelled brain shuttle peptide fusion dimeric affibody. Sci Rep. 2021;11(1):2588.
18. Ono M, Takahashi M, Shimozawa A, Fujinaga M, Mori W, Nagai Y, et al. In vivo visualization of propagating α-synuclein pathologies in mouse and marmoset models by a bimodal imaging probe, C05-05. 2020.
19. Roshanbin S, Xiong M, Hultqvist G, Söderberg L, Zachrisson O, Meier S, et al. In vivo imaging of alpha-synuclein with antibody-based PET. Neuropharmacology. 2022;208:108985.
20. Uzuegbunam BC, Librizzi D, Hooshyar Yousefi B. PET radiopharmaceuticals for Alzheimer's disease and Parkinson's disease diagnosis, the current and future landscape. Molecules. 2020; 25(4):977.
21. Verdurand M, Levigoureux E, Zeinyeh W, Berthier L, Mendjel-Herda M, Cadarossanesaib F, et al. In silico, in vitro, and in vivo evaluation of new candidates for α-synuclein PET imaging. Mol Pharm. 2018;15(8):3153–66.
22. Xiang J, Tao Y, Xia Y, Luo S, Zhao Q, Li B, et al. Development of an α-synuclein positron emission tomography tracer for imaging synucleinopathies. Cell. 2023;186:3350–3367.e19.
23. Klingstedt T, Ghetti B, Holton JL, Ling H, Nilsson KPR, Goedert M. Luminescent conjugated oligothiophenes distinguish between α-synuclein assemblies of Parkinson's disease and multiple system atrophy. Acta Neuropathol Commun. 2019;7(1):193.
24. Shahnawaz M, Mukherjee A, Pritzkow S, Mendez N, Rabadia P, Liu X, et al. Discriminating α-synuclein strains in Parkinson's disease and multiple system atrophy. Nature. 2020;578(7794):273–7.
25. Peelaerts W, Bousset L, Van der Perren A, Moskalyuk A, Pulizzi R, Giugliano M, et al. α-Synuclein strains cause distinct synucleinopathies after local and systemic administration. Nature. 2015;522(7556):340–4.
26. Price DL, Rockenstein E, Mante M, Adame A, Overk C, Spencer B, et al. Longitudinal live imaging of retinal α-synuclein:: GFP deposits in a transgenic mouse model of Parkinson's disease/dementia with Lewy bodies. Sci Rep. 2016;6:29523.
27. Liu XG, Lu S, Liu DQ, Zhang L, Zhang LX, Yu XL, et al. ScFv-conjugated superparamagnetic iron oxide nanoparticles for MRI-based diagnosis in transgenic mouse models of Parkinson's and Huntington's diseases. Brain Res. 2019;1707:141–53.
28. Chen Z, Zhou Q, Deán-Ben XL, Gezginer I, Ni R, Reiss M, et al. Multimodal noninvasive functional neurophotonic imaging of murine brain-wide sensory responses. Adv Sci. 2022;9(24): e2105588.
29. Deán-Ben XL, Robin J, Nozdriukhin D, Ni R, Zhao J, Glück C, et al. Deep optoacoustic localization microangiography of ischemic stroke in mice. Nat Commun. 2023;14(1):3584.
30. Razansky D, Distel M, Vinegoni C, Ma R, Perrimon N, Köster RW, et al. Multispectral opto-acoustic tomography of deep-seated fluorescent proteins in vivo. Nat Photon. 2009;3(7): 412–7.
31. Wang LV, Hu S. Photoacoustic tomography: in vivo imaging from organelles to organs. Science. 2012;335(6075):1458–62.
32. Ni R, Villois A, Dean-Ben XL, Chen Z, Vaas M, Stavrakis S, et al. In-vitro and in-vivo characterization of CRANAD-2 for multi-spectral optoacoustic tomography and fluorescence imaging of amyloid-beta deposits in Alzheimer mice. Photoacoustics. 2021; 23:100285.
33. Vagenknecht P, Luzgin A, Ono M, Ji B, Higuchi M, Noain D, et al. Non-invasive imaging of tau-targeted probe uptake by whole brain multi-spectral optoacoustic tomography. Eur J Nucl Med Mol Imaging. 2022;49:2137–52.
34. Naganuma F, Murata D, Inoue M, Maehori Y, Harada R, Furumoto S, et al. A novel near-infrared fluorescence probe THK-565 enables in vivo detection of amyloid deposits in Alzheimer's disease mouse model. Mol Imaging Biol. 2023;25:1115–24.
35. Giasson BI, Duda JE, Quinn SM, Zhang B, Trojanowski JQ, Lee VM. Neuronal alpha-synucleinopathy with severe movement disorder in mice expressing A53T human alpha-synuclein. Neuron. 2002;34(4):521–33.
36. Combes BF, Kalva SK, Benveniste P-L, Tournant A, Law MH, Newton J, et al. Spinal cord perfusion impairments in the M83 mouse model of Parkinson's disease. *bioRxiv*. 2024;2024-04.
37. Merlini M, Meyer EP, Ulmann-Schuler A, Nitsch RM. Vascular β-amyloid and early astrocyte alterations impair cerebrovascular function and cerebral metabolism in transgenic arcAβ mice. Acta Neuropathol. 2011;122(3):293–311.
38. Gotz J, Chen F, van Dorpe J, Nitsch RM. Formation of neurofibrillary tangles in P301l tau transgenic mice induced by Abeta 42 fibrils. Science. 2001;293(5534):1491–5.
39. Massalimova A, Ni R, Nitsch RM, Reisert M, von Elverfeldt D, Klohs J. DTI reveals whole-brain microstructural changes in the P301L mouse model of tauopathy. Neurodegener Dis. 2020; 20(5-6):173–84. https://doi.org/10.1101/2020.10.28.358465
40. Ni R, Zarb Y, Kuhn GA, Müller R, Yundung Y, Nitsch RM, et al. SWI and phase imaging reveal intracranial calcifications in the P301L mouse model of human tauopathy. MAGMA. 2020;33: 769–81.
41. Burmann BM, Gerez JA, Matecko-Burmann I, Campioni S, Kumari P, Ghosh D, et al. Regulation of alpha-synuclein by chaperones in mammalian cells. Nature. 2019;577:127–32.
42. Gerez JA, Prymaczok NC, Rockenstein E, Herrmann US, Schwarz P, Adame A, et al. A cullin-RING ubiquitin ligase targets exogenous alpha-synuclein and inhibits Lewy body-like pathology. Sci Transl Med. 2019;11(495):eaau6722.
43. Ni R, Chen Z, Gerez JA, Shi G, Zhou Q, Riek R, et al. Detection of cerebral tauopathy in P301L mice using high-resolution large-field multifocal illumination fluorescence microscopy. Biomed Opt Express. 2020;11(9):4989–5002.
44. Sobek J, Li J, Combes BF, Gerez JA, Nilsson PK, Henrich MT, et al. Efficient characterization of multiple binding sites of small molecule imaging ligands on amyloid-beta, tau and alpha-

synuclein. Eur J Nucl Med Mol Imaging. 2024;1–18. https://doi.org/10.1101/2023.03.12.531651
45. Ni R, Chen Z, Deán-Ben XL, Voigt FF, Kirschenbaum D, Shi G, et al. Multiscale optical and optoacoustic imaging of amyloid-β deposits in mice. Nat Biomed Eng. 2022;6:1031–44.
46. Prahl S. Optical Absorption of Hemoglobin. Available from: https://omlc.org/spectra/hemoglobin/. Accessed 10 Dec 2023.
47. Kecheliev V, Boss L, Maheshwari U, Konietzko U, Keller A, Razansky D, et al. Aquaporin 4 is differentially increased and dislocated in association with tau and amyloid-beta. Life Sci. 2023; 321:121593.
48. Yushkevich PA, Piven J, Hazlett HC, Smith RG, Ho S, Gee JC, et al. User-guided 3D active contour segmentation of anatomical structures: significantly improved efficiency and reliability. Neuroimage. 2006;31(3):1116–28.
49. Ono M, Sahara N, Kumata K, Ji B, Ni R, Koga S, et al. Distinct binding of PET ligands PBB3 and AV-1451 to tau fibril strains in neurodegenerative tauopathies. Brain. 2017; 140(3):764–80.
50. Raabe J, Tzvetkov G, Flechsig U, Böge M, Jaggi A, Sarafimov B, et al. PolLux: a new facility for soft x-ray spectromicroscopy at the Swiss Light Source. Rev Sci Instrum. 2008;79(11):113704.
51. Ma Y, Hof PR, Grant SC, Blackband SJ, Bennett R, Slatest L, et al. A three-dimensional digital atlas database of the adult C57BL/6J mouse brain by magnetic resonance microscopy. Neuroscience. 2005;135(4):1203–15.
52. Cox B, Laufer JG, Arridge SR, Beard PC. Quantitative spectroscopic photoacoustic imaging: a review. J Biomed Opt. 2012;17(6): 061202.
53. Dietrich O, Levin J, Ahmadi SA, Plate A, Reiser MF, Bötzel K, et al. MR imaging differentiation of Fe(2+) and Fe(3+) based on relaxation and magnetic susceptibility properties. Neuroradiology. 2017;59(4):403–9.
54. Schwab AD, Thurston MJ, Machhi J, Olson KE, Namminga KL, Gendelman HE, et al. Immunotherapy for Parkinson's disease. Neurobiol Dis. 2020;137:104760.
55. Dimant H, Kalia SK, Kalia LV, Zhu LN, Kibuuka L, Ebrahimi-Fakhari D, et al. Direct detection of alpha synuclein oligomers in vivo. Acta Neuropathol Commun. 2013;1(1):6.
56. Osterberg VR, Spinelli KJ, Weston LJ, Luk KC, Woltjer RL, Unni VK. Progressive aggregation of alpha-synuclein and selective degeneration of lewy inclusion-bearing neurons in a mouse model of parkinsonism. Cell Rep. 2015;10(8):1252–60.
57. Unni VK, Weissman TA, Rockenstein E, Masliah E, McLean PJ, Hyman BT. In vivo imaging of alpha-synuclein in mouse cortex demonstrates stable expression and differential subcellular compartment mobility. PLoS One. 2010;5(5):e10589.
58. Tzoumas S, Nunes A, Olefir I, Stangl S, Symvoulidis P, Glasl S, et al. Eigenspectra optoacoustic tomography achieves quantitative blood oxygenation imaging deep in tissues. Nat Commun. 2016;7: 12121.
59. Berg D, Gerlach M, Youdim MB, Double KL, Zecca L, Riederer P, et al. Brain iron pathways and their relevance to Parkinson's disease. J Neurochem. 2001;79(2):225–36.
60. Thomas GEC, Leyland LA, Schrag AE, Lees AJ, Acosta-Cabronero J, Weil RS. Brain iron deposition is linked with cognitive severity in Parkinson's disease. J Neurol Neurosurg Psychiatry. 2020;91(4):418–25.
61. Zucca FA, Segura-Aguilar J, Ferrari E, Muñoz P, Paris I, Sulzer D, et al. Interactions of iron, dopamine and neuromelanin pathways in brain aging and Parkinson's disease. Prog Neurobiol. 2017;155:96–119.
62. Dauer Née Joppe K, Tatenhorst L, Caldi Gomes L, Zhang S, Parvaz M, Carboni E, et al. Brain iron enrichment attenuates α-synuclein spreading after injection of preformed fibrils. J Neurochem. 2021;159(3):554–73.
63. Mamais A, Kluss JH, Bonet-Ponce L, Landeck N, Langston RG, Smith N, et al. Mutations in LRRK2 linked to Parkinson disease sequester Rab8a to damaged lysosomes and regulate transferrin-mediated iron uptake in microglia. PLoS Biol. 2021;19(12):e3001480.
64. Cong L, Muir ER, Chen C, Qian Y, Liu J, Biju KC, et al. Multimodal MRI evaluation of the MitoPark mouse model of Parkinson's disease. PLoS One. 2016;11(3):e0151884.
65. Barbosa JH, Santos AC, Tumas V, Liu M, Zheng W, Haacke EM, et al. Quantifying brain iron deposition in patients with Parkinson's disease using quantitative susceptibility mapping, R2 and R2. Magn Reson Imaging. 2015;33(5):559–65.
66. Drori E, Berman S, Mezer AA. Mapping microstructural gradients of the human striatum in normal aging and Parkinson's disease. Sci Adv. 2022;8(28):eabm1971.
67. Du G, Wang E, Sica C, Chen H, De Jesus S, Lewis MM, et al. Dynamics of nigral iron accumulation in Parkinson's disease: from diagnosis to late stage. Mov Disord. 2022;37(8):1654–62.
68. Graham JM, Paley MN, Grünewald RA, Hoggard N, Griffiths PD. Brain iron deposition in Parkinson's disease imaged using the PRIME magnetic resonance sequence. Brain. 2000; 123(Pt 12):2423–31.
69. Michaeli S, Oz G, Sorce DJ, Garwood M, Ugurbil K, Majestic S, et al. Assessment of brain iron and neuronal integrity in patients with Parkinson's disease using novel MRI contrasts. Mov Disord. 2007;22(3):334–40.
70. Wang C, Martins-Bach AB, Alfaro-Almagro F, Douaud G, Klein JC, Llera A, et al. Phenotypic and genetic associations of quantitative magnetic susceptibility in UK biobank brain imaging. Nat Neurosci. 2022;25(6):818–31.
71. Hare DJ, George JL, Grimm R, Wilkins S, Adlard PA, Cherny RA, et al. Three-dimensional elemental bio-imaging of Fe, Zn, Cu, Mn and P in a 6-hydroxydopamine lesioned mouse brain. Metallomics. 2010;2(11):745–53.
72. Jiang H, Song N, Xu H, Zhang S, Wang J, Xie J. Up-regulation of divalent metal transporter 1 in 6-hydroxydopamine intoxication is IRE/IRP dependent. Cell Res. 2010;20(3):345–56.
73. Zhai S, Tanimura A, Graves SM, Shen W, Surmeier DJ. Striatal synapses, circuits, and Parkinson's disease. Curr Opin Neurobiol. 2018;48:9–16.
74. Vermersch P, Leys D, Pruvo JP, Clarisse J, Petit H. Parkinson's disease and basal ganglia calcifications: prevalence and clinico-radiological correlations. Clin Neurol Neurosurg. 1992;94(3): 213–7.
75. Guo X, Hao H, Xing H, Guo Y. Idiopathic basal ganglia calcifications and Parkinson's disease. Am J Med. 2022;135:e368–9.

SUPPORTING INFORMATION

Additional supporting information can be found online in the Supporting Information section at the end of this article.

How to cite this article: Straumann N, Combes BF, Dean Ben XL, Sternke-Hoffmann R, Gerez JA, Dias I, et al. Visualizing alpha-synuclein and iron deposition in M83 mouse model of Parkinson's disease in vivo. Brain Pathology. 2024. e13288. https://doi.org/10.1111/bpa.13288